Journal of Energy Storage 45 (2022) 103516

Contents lists available at ScienceDirect

Journal of Energy Storage

journal homepage: www.elsevier.com/locate/est

Research Papers

Emergence of elevated battery positioning in air cooled battery packs for temperature uniformity in ultra-fast dis/charging applications

Sinan Gocmen, Erdal Cetkin *

Department of Mechanical Engineering, Izmir Institute of Technology, Turkey

ARTICLE INFO

Keywords:
Battery pack thermal management
NTGK model
Ultra-fast discharging
Temperature uniformity
Forced air convection

ABSTRACT

Pure electric vehicles (EVs) are gradually becoming major interest of research in worldwide. Battery cells in EV battery packs must be kept in between the desired operational temperature range (~30°C) and temperature should be homogeneous in packs to eliminate safety risks and prolong battery life. In this study, performance of a novel BTMS design was studied at various discharge conditions with fast and ultra-fast C-rate values. Cooling with natural convection exceeds desired operational temperature in the pack as well as forced air convection in Z-type manifold. Elevated battery positions yield flow resistance along the air channels in between battery cells to be uniform which yields flow rate sweeping the surface of each cell to be the same. Therefore, the maximum temperature in between cells decreases to less than 0.3K from the order of 12K. The temperature uniformity is essential for ageing and electrical resistance of cells to be homogeneous in a pack. In addition, heat transfer enhancement with various fin designs is documented as well as its effect on the temperature distribution. The accuracy of numerical studies is validated by experimental work. The results show that the peak temperature can be kept under the desired operational temperature with minimum deviation in the temperature difference for distinct operation conditions required for advanced electric vehicles (cars, airplanes, helicopters) with extreme charging and discharging capability.

1. Introduction

Internal combustion engines become obsolete because of their major responsibility in environmental pollution. During Covid-19 pandemic, demand on transportation had declined greatly which yielded the air quality increase in densely populated cities. In addition, many countries and cities plan to ban the use of internal combustion vehicles locally or nationally in the next decade. Pure electric vehicles are more efficient in comparison to internal combustion vehicles (if the efficiency calculated from power plant and fossil fuel well to the work being done during mobility) and their effect on the environment is a lot less especially electricity generated via renewable sources. In general, the leading electric vehicle manufacturers prefer the lithium-ion batteries (LIBs) because of their high energy density, low self-discharge rate, being light, no memory effect and longer life cycle [1–3]. However, there are also major drawbacks such as range, charging time, and capacity fade. Hence, the research and development studies are concentrated to improve the battery characteristics and the operating conditions [4–6]. Generated heat during charge/discharge and heating requirement for cold climates result with temperature variation in battery packs. Heat generation mechanisms can be expressed as Joule effect, electrochemical reactions, side reactions and polarization reactions [7]. It is desirable to convert all the battery energy stored in the battery into useful electrical energy. However, losses occur due to polarization when current flows through the electrodes. These losses are a result of ohmic polarization, activation polarization and concentration polarization effects [8,9]. In general, as the temperature increases, the effects of ohmic, concentration and kinetic polarization decreases. Thus, the capacity increases with the cell potential, but in some uncommon cases, the capacity may decrease due to increased self-discharge [10]. However, battery life and performance are also significantly affected by increased temperature [11]. This demonstrates the importance of ensuring an optimal trade-off between temperature and polarization effects. Therefore, advanced thermal management systems with strict temperature control is required to keep temperature in the desired range to eliminate safety risks (thermal runaway) and capacity fade related with temperature exceeding the desired temperature range especially in ultra-fast charging and discharging [12–15]. For instance, many fatal accidents occurred in distinct applications where LIBs are used [16,17]. Therefore, literature documents numerous studies with the aim of designing a proper battery thermal management system via simulating

* Corresponding author.
E-mail address: erdalcetkin@iyte.edu.tr (E. Cetkin).

https://doi.org/10.1016/j.est.2021.103516
Received 21 February 2021; Received in revised form 28 June 2021; Accepted 27 October 2021
Available online 8 November 2021
2352-152X/© 2021 Elsevier Ltd. All rights reserved.

Nomenclature

$\overline{P}$	average pressure [Pa]
Q_{nom}	total electric capacity [Ah]
Q_{ref}	reference capacity [Ah]
$\overline{T}$	average temperature [K]
T_{ref}	reference temperature [K]
c_p	specific heat capacity [J kg^{-1} K^{-1}]
$\dot{m}$	mass flow rate [kg s^{-1}]
$\dot{q}$	heat generation rate [W]
$\overline{u}$	average velocity component in each direction [m s^{-1}]
H_{in}	height of inlet region [mm]
H_{out}	height of inlet region [mm]
j_{ECh}	volumetric current transfer rate
j_{short}	current transfer rate
k	turbulent kinetic energy [m^2 s^{-2}]
L_{in}	length of the inlet region [mm]
L_{out}	length of the outlet region [mm]
P	pressure [Pa]
t	time [s]
T	temperature [K]
u`	fluctuations of velocity in each direction [m s^{-1}]
u	velocity vector [m s-1]
W_{in}	width of the inlet region [mm]
W_{out}	width of the outlet region [mm]
λ	conductivity [W/mK]
DoD	depth of discharge
Vol	volume of the active zone
x	component of the coordinate system [m]

Greek letters

ΔT	temperature difference [K]
ε	turbulent kinetic energy dissipation rate [m^2 s^{-3}]
μ	viscosity [Pa s]
ρ	density [kg m^{-3}]
σ_k	turbulent Prandtl number for k [dimensionless]
σ_ε	turbulent Prandtl number for ε [dimensionless]
σ_{cp}	turbulent Prandtl number based on specific heat at constant pressure [dimensionless]
σ_+	effective electric conductivity for the positive electrodes
σ_-	effective electric conductivity for the negative electrodes
φ_+	phase potential of positive electrodes
φ_-	phase potential of positive electrodes

electrochemical behavior of cells with the thermal characteristics of them.

Doyle et al. modeled a galvanostatic charge and discharge of a lithium polymer cell using by concentrated solution theory [18]. Chen and Evans developed two dimensional and three-dimensional models to examine the behaviors of lithium polymer and lithium-ion batteries at various C-rates [19–21]. Wang et al. developed thermal and electrochemical models for LIBs which are two-dimensional [22]. Kwon et al. examined the potential and current density distribution on the electrodes of a LIB with the model they had developed at 25 °C ambient temperature [23]. Kim et al. also presented two-dimensional thermal model to show the dependence of the discharge behavior of a LIB on the variation of ambient temperature [24]. The literature shows the performance, safety and lifetime of the batteries depend on their operating temperature. Therefore, effective and efficient BTMS designs play an integral role in the advancement of the EV technology. For instance, operation temperature should be strictly in between 288 K and 308 K [25], for a specific chemistry. Therefore, the literature documents many distinct BTMS designs with various thermal management techniques. In general, these can be categorized as active and passive BTMSs. Active systems require external source for circulation of a working fluid to keep the batteries in the optimal temperature range while the passive ones do not as they rely on latent heat requirement being comparatively great during phase change (heat pipe or PCM) [26–32]. In addition, air cooled BTMSs become the best option for some specific applications due to their advantages such as simplicity, low-cost, no risk for electric shortage and being lighter (no liquid tank, pump, cold plate, piping etc.). Besides these advantages, air cooling is rarely used in EV applications compared to liquid cooling, except for some popular vehicles such as Leaf, E-Golf, Zoe 40 and Prius [33]. Poor thermal conductivity and heat capacity of air and that achieving uniform air distribution in the pack is more difficult than liquid cooling are the main reasons why liquid cooling is widely preferred over air cooling. Homogeneous distribution of the battery cell temperatures will be ensured by the homogeneous distribution of air between the cell surfaces. Thus, this main obstacle can be overcome and the advantages of air cooling may be appreciated. For instance, Sun and Dixon developed a three-dimensional battery pack thermal model and showed that Z-type manifold reduce the fluctuation in the temperature distribution [34]. Cetkin presented how the microdevice manifold design should be in order to provide uniform flow rate distribution for each manifold channel using constructal theory [35]. Similarly, a wedge shaped runner was proposed in a study to improve temperature homogeneity [36]. Zhang et al. examined that the structure of wedge-shaped runner and the position of the inlet and outlet. The results of the study showed that the maximum temperature of the cells and temperature difference between the cells were kept below 313 K and 2 K, respectively. Wang et al. uncovered the effect of various forced-air cooling strategies with 3-D CFD models. Their results showed that forced air-cooling can decrease the maximum temperature in the pack, and the axisymmetric model is thermally the most efficient case in comparison to the competing designs in their research [37]. Chen et al. have documented the effect of some parameters on the structure of air-cooled BTMS to provide better cooling performance [38]. For parallel air-cooled BTMSs with Z-type, U-type and I-type flows, Zhang et al. developed a transient heat transfer model [39]. In the study where experiments were carried out to demonstrate the effectiveness of the developed models, it was revealed that the maximum temperature and temperature difference deviations decreased by 70% and 26%, respectively, compared to previous study. Pan et al. investigated uniform flow distribution in parallel air-cooled structure [40]. Numerically and experimentally supported results show that the average temperature difference was kept around 1.4 °C which is 50% of traditional structure by adding a fan on bottom of the 3 × 4 cylindrical battery pack. Maharudrayya et al. examined the dimensionless flow distributions of the U-type and Z-type manifold models. Their study reveals that the dimensionless velocity distribution between the manifold channels does not vary with volume flow rate, i.e. the trend is almost the same [41]. Xu and He performed numerical analysis for various airflow duct models such as horizontal, longitudinal, and U type. They improved the heat dissipation performance of a battery pack design. Their results showed that longitudinal battery pack design conforms more uniform temperature distribution in comparison to the horizontal one. However, it does not satisfy the safety criteria, and thus U-type was also evaluated. They recommended double U-type duct design as the first choice for air-cooled battery pack designs. In another heat dissipation and optimization study, Li et al. studied a cooling method with herringbone fins and long sleeves [42]. The study showed that the maximum temperature and the maximum temperature difference were decreased by 0.69 K and

17.92%, respectively, considering cooling cost.

Overall, literature documents that temperature uniformity in pack level is not in the desired level. This study focus on uncovering pack designs with temperature uniformity in between battery cells and also along them. First, z-type manifold design (Fig. 1(a)) which had been developed in our previous work [43] was simulated by using Newman, Tiedeman, Gu and Kim (NTGK) electrochemical battery model, which provides more realistic results due to its heat generation approach in a battery cell. Electrochemical model was simulated with fluid and heat flow simultaneously in battery pack level. In three-dimensional CFD simulations, 14.6 Ah lithium-ion pouch cells were used, and they were connected in series (15S1P) to form a battery pack. The simulations document the effect of inlet air velocity (2, 4, 6, 8 and 10 m/s) as discharge rate vary (5C, 6C, 8C and 10C). In addition, the effect of fins on temperature distribution was also documented.

2. Model and method

Satisfying optimum operational temperature range in batteries is crucial for safety and extending battery life. Thus, it is a great advantage to have an estimation of heat generation of cells during discharge/charge during the development of advanced battery thermal management systems. Therefore, in this study, Newman, Tiedeman, Gu and Kim (NTGK) semi-empirical electrochemical battery model was incorporated with multi scale multi domain (MSMD) approach in ANSYS Fluent. Current study yields a realistic approach to mimic the behavior of cells under operation to uncover the performance of the manifold design developed in our previous study for forced air convection [43]. The proposed manifold design, the illustration and structural properties of which are given in Fig. 1(a) and Table 1, respectively, provides uniform temperature distribution among the battery cells by distributing the air into cooling channels evenly. Unlike our previous work, heat generation in cells are non-uniform and time dependent as it relies on the electrochemical model incorporated with the thermal model.

Here, a three-dimensional model of a lithium-ion pouch cell with its geometry and dimensions are given in Fig. 1(b) was developed. The properties of the battery cell and cooling air are listed in Table 2. In the electrochemical battery model formulation, the volumetric current transfer rate is defined by the following equation [23,44]:

Table 1
Structural properties of manifold design.

Parameters	Value [mm]
Length of the inlet region (L_{in})	100
Height of inlet region (H_{in})	100
Width of the inlet region (W_{in})	192
Length of the outlet region (L_{out})	100
Height of the outlet region (H_{out})	50
Width of the outlet region (W_{out})	192

Table 2
Physical properties of battery cell and air.

Parameter	Battery Cell	Air@298 K
Density (kg/m^3)	2092	1.184
Specific heat capacity (J/(kg.K))	678	1007
Thermal conductivity (W/(m.K))	18.2	0.02551
Dynamic viscosity (kg/(m.s))	-	1.149E-5
Size (mm)	7 × 145 × 192	-

$$j_{ECh} = \frac{Q_{nominal}}{Q_{ref} Vol} Y \left[U - (\varphi_+ - \varphi_-)\right] \tag{1}$$

where $Q_{nominal}$ denotes total electric capacity of the cell, Q_{ref} is the capacity of the battery used in experiments, Vol describes volume of the active zone, φ_+ and φ_- terms are phase potentials for positive and negative electrodes. U and Y are the fitting parameters, and they are defined as a function of the battery depth of discharge (DOD) [45]. U and Y functions can also be determined by the curve that fits the voltage-current curve obtained from the experiments for a battery cell. In the formulation, the following equations were suggested by ANSYS Fluent [44]:

$$U = \left(\sum_{n=0}^{5} a_n (DoD)^n\right) - C_2 (T - T_{ref}) \tag{2}$$

$$Y = \left(\sum_{n=0}^{5} b_n (DoD)^n\right) exp\left[-C_2\left(\frac{1}{T} - \frac{1}{T_{ref}}\right)\right] \tag{3}$$

where a_n and b_n are the constants obtained from experiments, C_1 and C_2

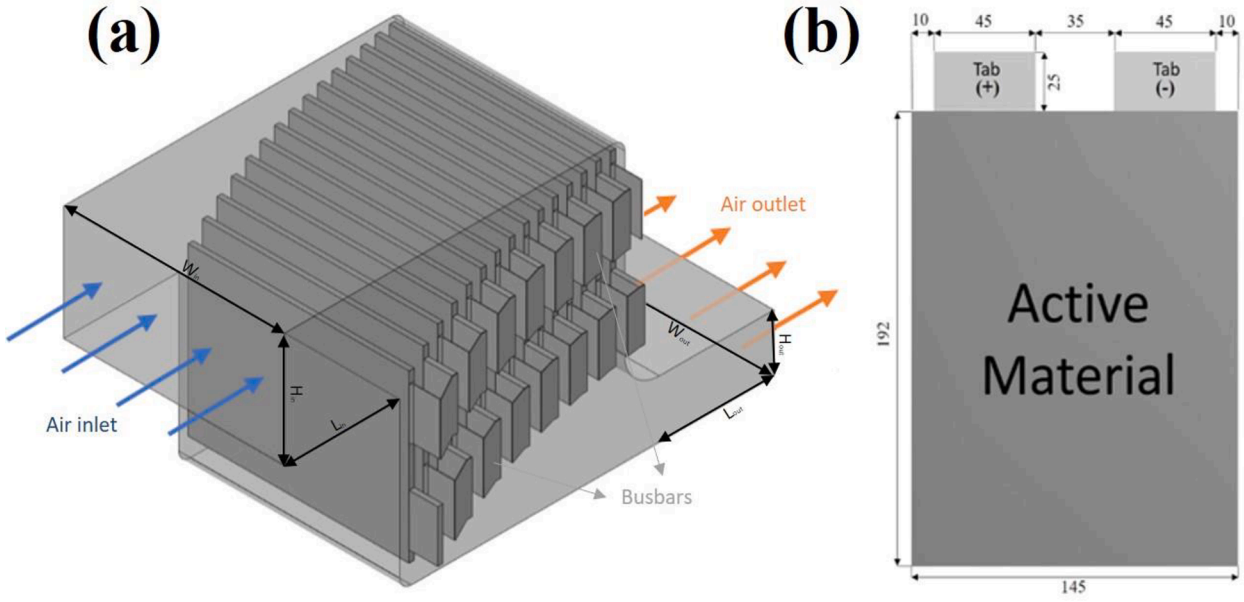

Fig. 1. (a) Developed manifold design and (b) battery model domain.

denote the NTGK model constants. The electrochemical reaction heat $\dot{q}_{ECh}$, which consists of electrochemical reactions in the model, is calculated as

$$\dot{q}_{ECh} = j_{ECh}\left[U - (\varphi_+ - \varphi_-) - T\frac{dU}{dT}\right] \tag{4}$$

where the first term represents heat due to overpotential and the other is heat based on entropic heating [44].

Fig. 1(a) shows the numerical domain of proposed manifold design [43]. Air enters from inlet of the manifold at ambient temperature of 298K. It is distributed along the cooling channels uniformly thanks to its unique design. Then, it leaves the manifold from outlet port at atmospheric conditions. Fluid flow is incompressible and turbulent for the cases with air velocity greater than 2 m/s. Fluid flow solved with time-dependent solvers to eliminate possible flow fluctuations due to time dependent heat generation. The conservation of mass and momentum are [44]

$$\frac{\partial \rho}{\partial t} + \frac{\partial}{\partial x_i}\left(\rho \overline{u}_i\right) = 0 \tag{5}$$

$$\frac{\partial}{\partial t}\left(\rho \overline{u}_i\right) + \frac{\partial}{\partial x_j}\left(\rho \overline{u}_i \overline{u}_j\right) = -\frac{\partial \overline{p}}{\partial x_i} + \frac{\partial}{\partial x_j}\left[\mu\left(\frac{\partial \overline{u}_i}{\partial x_j} + \frac{\partial \overline{u}_j}{\partial x_i} - \frac{2}{3}\delta_{ij}\frac{\partial \overline{u}_m}{\partial x_m}\right)\right] + \frac{\partial}{\partial x_j}\left(-\rho\overline{u'_i u'_j}\right) \tag{6}$$

where ρ, $\overline{u}_i$, u'_i, $\overline{p}$, μ are density, mean velocity component, fluctuating velocity component, mean pressure, and dynamic viscosity, respectively. k-ε turbulent model was chosen as viscous turbulent model, and it is calculated by following equations,

$$\frac{\partial(\rho k)}{\partial t} + \frac{\partial}{\partial x_i}\left(\rho k \overline{u}_i\right) = \frac{\partial}{\partial x_j}\left[\left(\mu + \frac{\mu_t}{\sigma_k}\right)\frac{\partial k}{\partial x_j}\right] \pm \rho\overline{u'_i u'_j}\frac{\partial u_j}{\partial x_i} - \rho\varepsilon \tag{7}$$

$$\frac{\partial(\rho \varepsilon)}{\partial t} + \frac{\partial}{\partial x_i}\left(\rho \varepsilon \overline{u}_i\right) = \frac{\partial}{\partial x_j}\left[\left(\mu + \frac{\mu_t}{\sigma_\varepsilon}\right)\frac{\partial \varepsilon}{\partial x_j}\right] + C_1\frac{\varepsilon}{k}\left(-\rho\overline{u'_i u'_j}\frac{\partial u_j}{\partial x_i}\right) - C_2\rho\frac{\varepsilon^2}{k} \tag{8}$$

$$\mu_t = \rho C_\mu \frac{k^2}{\varepsilon} \tag{9}$$

where $\mu_t, \varepsilon,\ k,\ C_\mu,\ \sigma_k$and σ_ε are eddy viscosity, eddy dissipation rate, turbulence energy term, empirical coefficient and turbulent Prandtl numbers for k and ε, respectively, which are $C_\mu = 0.09,\ C_1 = 1.44,\ C_2 = 1.92,\ \sigma_k = 1$ *and* $\sigma_\varepsilon = 1.3$ [44]. Regarding NTGK battery model, battery thermal and electrical fields were calculated in numerical domain by following equation [44]

$$\frac{\partial\left(\rho C_p T\right)}{\partial t} - \nabla.(k\nabla \mathrm{T}) = \sigma_+|\nabla\varphi_+|^2 + \sigma_-|\nabla\varphi_-|^2 + \dot{q}_{ECh} \tag{10}$$

where T *and* λ are temperature and thermal conductivity, respectively. σ_+ and σ_- denote the effective electric conductivities for the positive and negative electrodes.

Table 3 shows the effect of mesh size on simulations. In the mesh structure, two element types (hexahedral for the battery domain and tetrahedral for the flow domain) were used. The element size, inflation number and layer thickness were varied in order to results to become independent of mesh size even for the regions where the gradients almost does not change. The effect of mesh size on the maximum temperatures of air at the outlet and batteries with relative errors can be seen in Table 3. Consequently, the mesh structure which has approximately 9822385 elements with 5 inflation layer (0.1 mm first inflation layer thickness) yields results free of mesh size, i.e. relative error less than 0.01%.

Current battery model results validated by the results of Kim et al. [24] where dimensions, materials, thermal and electrochemical properties are identical. Results of our numerical model was compared with experimental and numerical data of their study. Fig. 2(a) shows the maximum temperature change with respect to time and voltage-capacity curve for a single battery cell at 298 K ambient temperature for three distinct C-rates: 1C, 3C and 5C. For all discharge cases, the maximum temperature deviation from Kim's experimental and numerical data is ±1.5 K, cf. Fig. 2(a). Moreover, the voltage-capacity curves show the results of the current study are in agreement with the results of Ref. [24], Fig. 2(b). These results show that our current numerical approach is valid.

Table 3
Effect of mesh size on simulation results.

	Temperature [K]		Relative Error (%)	
Number of Mesh Elements	Maximum Outlet	Maximum Battery	Maximum Outlet	Maximum Battery
863925	304.078	304.441		
1401807	302.448	302.855	0.5361	0.5208
5234692	303.150	303.143	0.2319	0.0950
8726784	303.200	303.198	0.0167	0.0181
9822385	303.334	303.315	0.0441	0.0387
12903540	303.315	303.332	0.0061	0.0056

3. Results and discussion

The effect of inlet velocity and temperature as well as distribution of air into the battery pack volume are essential for air cooled battery packs. Firstly, three dimensional simulations for discharging the battery pack (15S1P) at C-rates of 5C, 6C, 8C and 10C without forced convection were conducted to uncover the maximum temperatures and hotspot locations which may occur on the batteries. In general, although electric cars do not need such high discharge rates of 10C during normal operation, electric vehicles such as electric aircraft and electric helicopters require to reach these rates instantaneously, especially during climbing [46]. Besides, the charge rate is expected to increase to these values during extreme-fast charging of battery packs. In addition, investigation of battery characteristics at high discharge rates is gaining importance in the literature [47–49].

Fig. 3(a) shows the temperature distribution on the battery pack surface without active cooling at 10C where the maximum temperature is 348K. Maximum temperature occur near the tabs which confirms the results documented in the current literature. Moreover, the maximum temperature difference between the batteries in the pack increases up to 14K. Fig. 3(b) shows the evolution of the peak temperature in time for C-rates of 5, 6, 8 and 10. Peak temperature curve becomes steeper as the C-rate increases. For the given battery configurations, minimum and maximum peak temperatures occurring at the end of discharge are 317K and 348K. These results uncover that without active cooling desired operation temperature cannot be achieved even there would be no inconsistency in between battery cells and no unpredictable situation. Therefore, active cooling in battery packs is a must.

Furthermore, an air-cooled battery pack (15S1P) with base design was simulated to document the variation of the flow rate distribution on the temperature distribution. The validated li-ion battery model was inserted into the base manifold design. Nominal capacity and voltage of each cell in the manifold are 14.6 Ah and 4.2 V, respectively. Three-dimensional simulation was performed at 10C discharge rate and 298 K ambient temperature. Accordingly, Fig. 4(a) shows the temperature distribution for the base manifold design. The figure shows that the maximum battery temperature of 316.3 K is obtained in the first cell. In addition, the maximum battery temperature difference in the pack is 12.15 K. The flow rates in each channel are given in Fig. 4(b). The flow rates vary between the entrance and exit, as the pressure gradient changes greatly. The results of three-dimensional simulations in Fig. 4

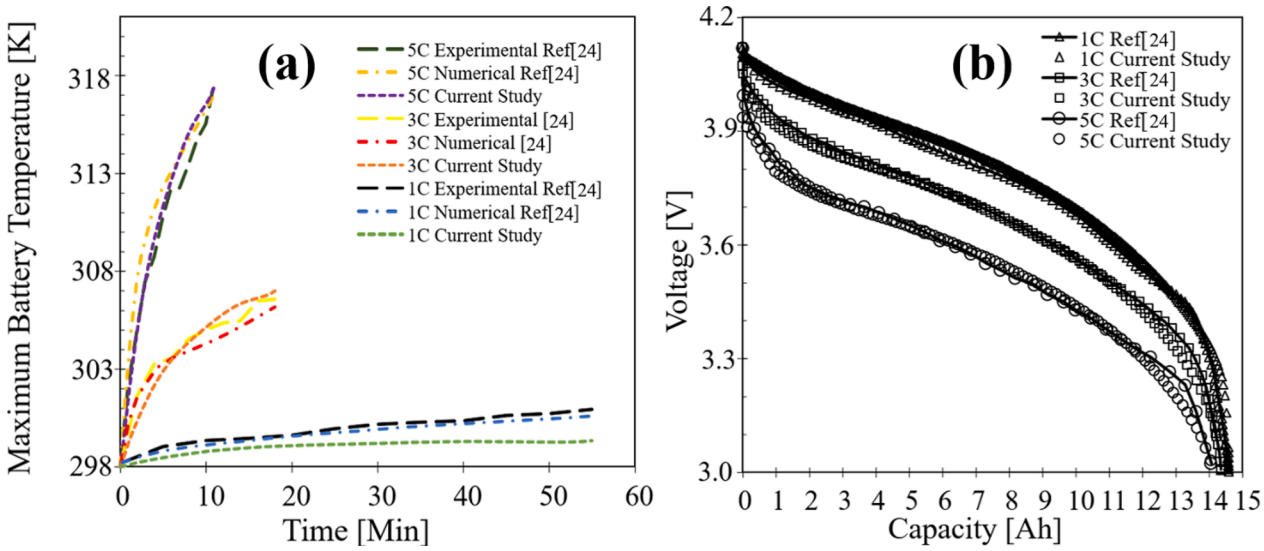

Fig. 2. Comparison of (a) maximum battery temperatures and (b) voltage curves of Ref. [24] and current study for 1C, 3C and 5C at 298K.

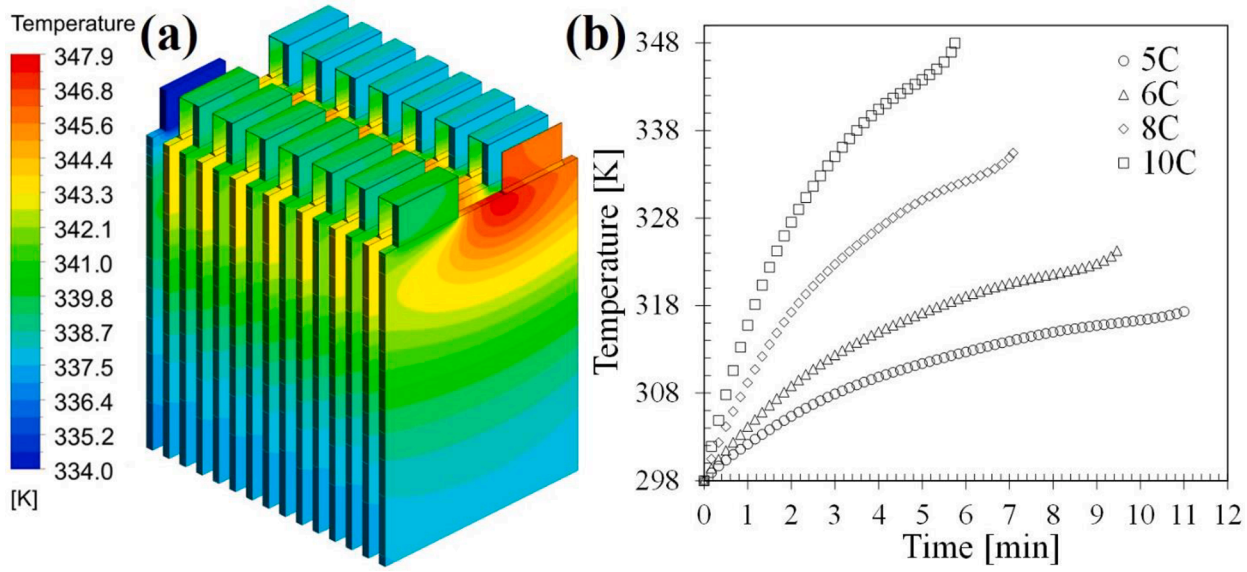

Fig. 3. (a) Temperature distribution in a 15S1P battery pack at 10C without forced-convection and (b) maximum temperature in the pack for 5C, 6C, 8C and 10C discharge rates.

show that the temperature distribution in battery pack is affected greatly from non-uniformity of flow rate. The maximum temperature difference in between batteries increases as the flow rate deviation between the channels becomes greater. Therefore, the coolant must be uniformly distributed along the channels to provide temperature uniformity between the batteries.

The developed manifold design (Fig 1(a)) which was uncovered in our previous study [43] was used to distribute the flow rates in each channel uniformly. In addition, the effect of inlet velocities on the flow rate distribution and temperature distribution were investigated by conducting additional simulations which include five distinct inlet velocities (2, 4, 6, 8 and 10 m/s). Fig. 5(a) documents that the flow rates in each channel in the manifold were distributed uniformly for all air inlet velocities. The average flow rate deviations from the average flow rates in each case are less than 2%. In addition, the flow rate with velocity of 10 m/s is more uniform relative to other cases (the maximum deviation 0.98%, channel #16).

However, Fig. 5(a) also documents maximum flow rate deviations in last two channels gradually increase as the inlet velocity decreases. The maximum flow rate deviations from the average flow rate rise to 13.1 and 9.8% in the channels of #16 and #15, respectively. Except the last two channels, the average flow rate deviation from the average flow rate is approximately 1.3%. Overall, Fig. 5(a) shows that the flow rates along each channel is almost the same. The results also shows that flow rate distribution along the channels is not affected greatly from the inlet velocity for the manifold design especially when the velocity magnitude becomes more than 8 m/s. Uniform flow rate distribution is focused as it reduces the maximum cell temperature and enhances temperature uniformity in the battery pack by eliminating under and over cooled regions. Accordingly, Fig. 5(b) shows that the flow uniformity along the channels is provided by the nearly same pressure differences in between inlet and outlet of each channel thanks to constructal design. Despite the fact that the pressure distribution varies greatly between the inlet and outlet sections of channels, the pressure gradient is kept almost constant.

Fig. 5 also reveals that even the uniformly distributed air flow with maximum inlet velocity of 10 m/s cannot keep the batteries between the

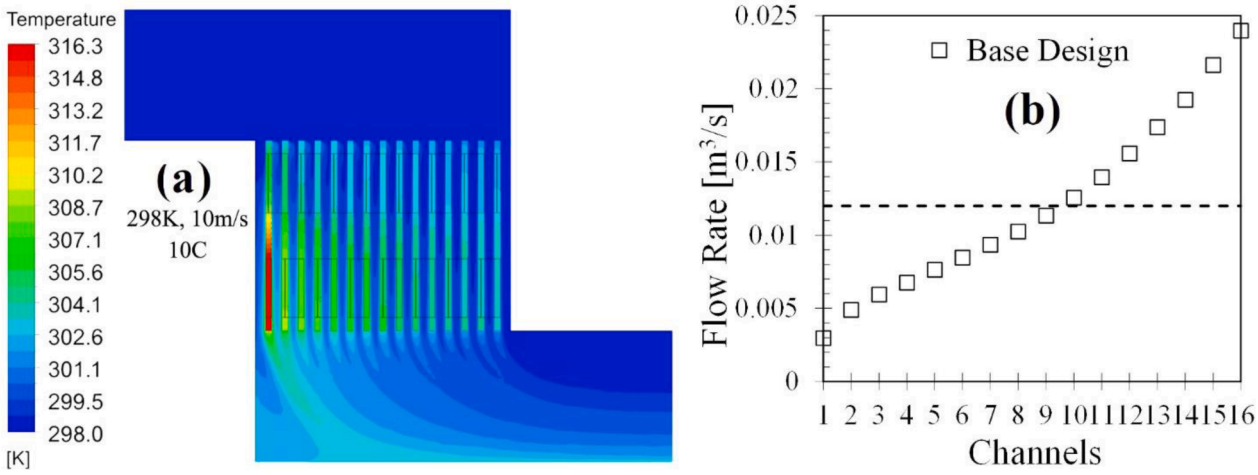

Fig. 4. (a) Temperature distribution of base design at 10C with inlet velocity of 10 m/s and (b) flow rates in each channel.

desired temperature range at 10C discharge rate for both inlet air temperatures of 298 K and 303 K. The maximum temperatures on the cells are increased up to 312.4 K and 316.9 K, respectively, as can be seen in Fig. 5(c) and (e). Furthermore, the maximum temperature differences between the batteries are 9.2 K and 8.8 K. On the other hand, Fig. 5(d) and (f) show that the series battery connections cause the repeated small fluctuation on the maximum battery temperatures due to the high discharge rates and the concentration of the heat generation nearby the positive tabs. The fluctuation on the temperatures can be prevented in experimental applications by locating the batteries same direction and using longer busbars. However, in the numerical simulations based on Ansys Fluent, this type of solution may cause unpredictable discharge behaviours. To sum up, it is obvious that the air cooling at high discharge rates will not be adequate. Therefore, integration of longitudinal fins to the battery surfaces is considered to increase the heat transfer rate from the cells. Accordingly, the governing equations were solved for the air flow between two battery cells with fins to investigate the effect of the fin structures constructed of aluminium with thermal conductivity 202.4 $Wm^{-1}K^{-1}$.

Firstly, 26 aluminium fins of 1 mm thickness were placed with three distinct lengths (1 mm, 2 mm and 3 mm) as well as no fin case on aluminium plate of 1 mm thickness in order to distribute the temperature more uniformly and to increase the heat transfer rate. Air enters from the long side of the computational domain at 298 K with minimum chosen velocity of 2 m/s and leaves from the other side to atmospheric conditions. The batteries were connected in series, also discharged at 10C discharge rate. The temperatures (maximum, mean and minimum) and the pressure drops for all cases are listed in Table 4, and also Fig. 6 (a)–(c) show the temperature distributions obtained from three-dimensional numerical analysis which are performed for the cases without fin structure, with just aluminium plate structure and with the optimum fin structure option.

In the absence of fin structure, the maximum temperature and the maximum temperature difference on the cells are 321.04 K and 9.98 K, respectively, also cf. Fig. 6(a). The addition of fins with 1 mm length reduces the maximum temperature and maximum temperature difference to 314.99 K and 3.32 K as can be seen in Table 4. Comparison of fin lengths of 2 mm and 3 mm shows that the peak temperature on the cells and the temperature difference are decreased from 313.82 K to 313.59 K and from 3.46 K to 3.2 K. Since the characteristic length with 3mm fins are very small in comparison to the others, the flow becomes internal flow which affect the pressure drop. Therefore, the pressure drop is measured less in the case of the 3 mm fin. Therefore, the best case with fin length of 3 mm was selected to continue with simulations to uncover the effect of number of fins. In order to evaluate the effect of number of fins, three distinct numbers (13, 26 and 39) of fins on aluminium plate of 1 mm thickness were chosen. The results given in Table 4 show that all the temperatures decrease as the number of fins increase, however, the flow resistance increases proportionally through the split channels where the air flow is provided. Therefore, the case with a fin number of 26 with a maximum temperature of 313.6 K and a pressure drop of 13.6 Pa was chosen to investigate the effect of fin thickness. Finally, three distinct thicknesses (0.5 mm, 1 mm and 2 mm) were selected to uncover thickness effect. Comparison of the results show that the maximum temperature on the cells and temperature difference are decreased to 313.03 K and 2.65 K, respectively. However, considering the trade-off between the cases, the case with thickness of 1 mm was decided as the best option where the temperature values are not affected greatly from the variation of thickness in the given range. Consequently, the maximum battery temperature and temperature distribution on the batteries are affected apparently from the fin length. Therefore, integrating 26 fins with length of 3 mm and thickness of 1 mm into the manifold design was decided, and the analysis of this design was performed at 10C discharge rate with chosen inlet velocities.

Fig. 7(a)–(d) show the temperature distributions at the end of the discharge processes for the no-fin and with integrated 3 mm long fin structure cases with inlet velocity of 10 m/s at 298 K and 303 K, respectively. Comparison of Fig. 7(a) and (b) shows that the maximum battery temperature and temperature difference between the cells are reduced by 8.5 K and 6.6 K thanks to integrating fin structure relative to the manifold design with no fin structure. The addition of fin structure provides that the maximum temperature difference between the peak temperatures observed in the battery cells is around 0.15 K, and the maximum temperature difference on a single cell varies below 2.2 K for all cells (Fig. 7(b)). Overall, the maximum temperatures in the pack are kept between the desired temperature range for inlet air temperature of 298 K. On the other hand, Fig. 7(c) and (d) show that the maximum cell temperature reduced by 8.5 K and the desired temperature limit is almost achieved, less than 0.28 K difference, for the case with inlet air temperature of 303 K. Therefore, the manifold design with fins can be assumed to provide adequate performance in terms of cooling capability.

However, the flow rate distributions in the channels are adversely affected by the addition of fins relative to no-fin case. The opposite fins on batteries divide the channels to smaller air ducts (except channel #1 and #16). This situation causes the flow resistance to increase along the channels. Fig. 7 (e) shows the flow rates in the first and last three channels are deviated from average flow rate by maximum 5.8% and 8.4% (channel #2 and #15) compared to no-fin case, respectively. Nevertheless, the flow rates between the rest of channels are uniformly distributed and the average flow rate deviation between the channels is 2.3%. On the other hand, Fig. 7(f) documents temperature distribution

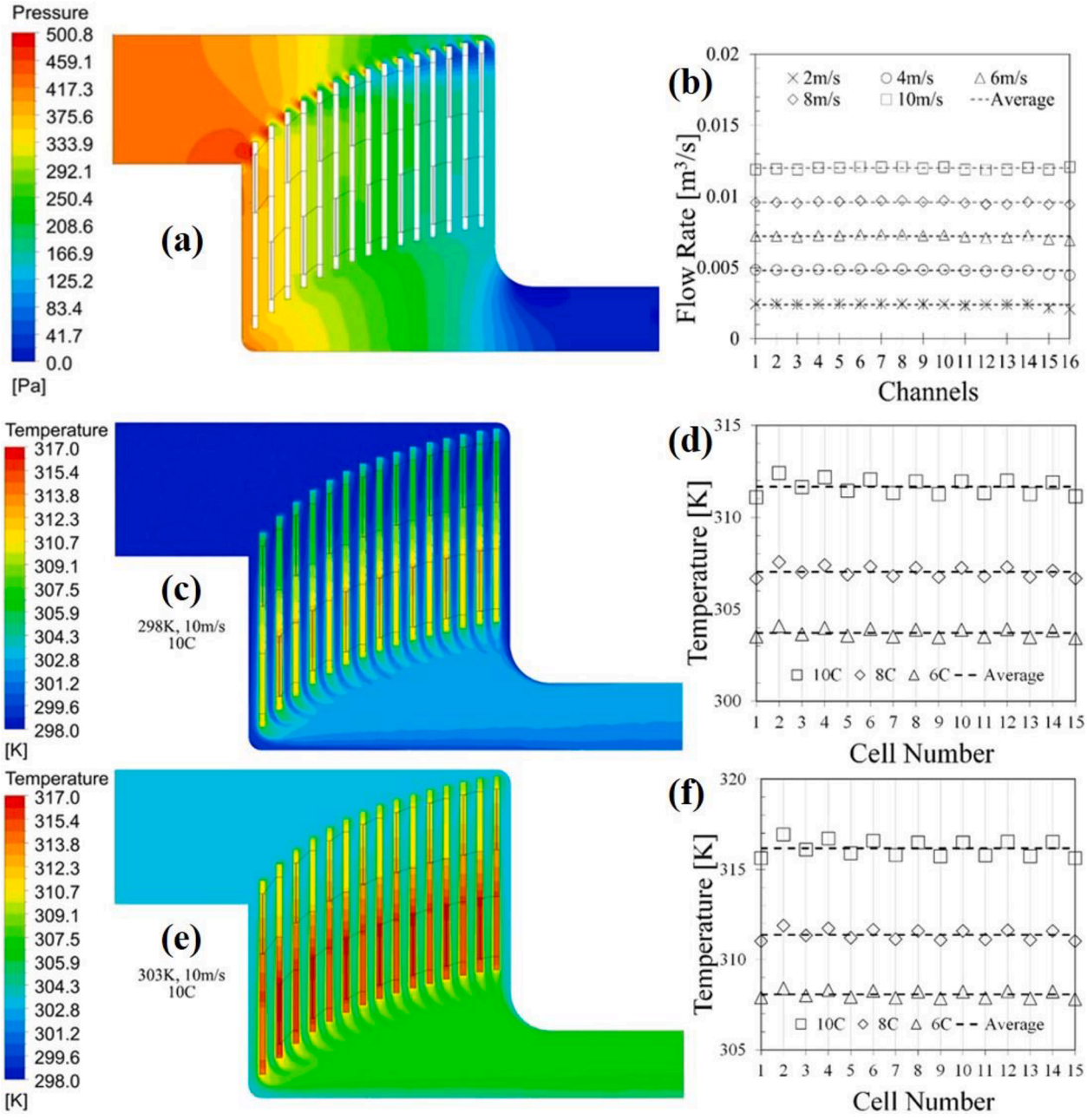

Fig. 5. (a) Flow rate along each channel for all inlet velocities and (b) Pressure distribution for inlet velocity of 10 m/s, (c) Temperature distribution of battery pack at 10C discharge rate and (d) maximum battery temperatures in the pack at 6C,8C and 10C for the inlet conditions of 298 K and 10 m/s, (e) temperature distribution of battery pack in the manifold at 10C discharge rate and (f) maximum battery temperatures in the pack at 6C,8C and 10C for inlet conditions of 303 K and 10 m/s.

Table 4
Thermal and hydraulic results for the fin study.

Cases [Number.Length. Thickness]	Battery no.1			Battery no.2			Air.Temp. [K]		Pressure Drop [Pa]
	Max. Temp. [K]	Mean Temp. [K]	Min. Temp. [K]	Max. Temp. [K]	Mean Temp. [K]	Min. Temp. [K]	Outlet (Mean)	Inlet	
No-fin.No-plate	321.019	316.517	311.038	321.036	316.698	312.13	306.935	298	4.01
No-fin.With-plate	316.389	314.957	312.953	316.422	315.004	313.415	307.435	298	5.28
26.1[mm].1[mm]	314.959	313.552	311.643	314.986	313.585	312.013	307.707	298	12.282
26.2[mm].1[mm]	313.819	312.3	310.36	313.815	312.319	310.64	308.712	298	15.686
26.3[mm].1[mm]	313.588	312.134	310.39	313.588	312.132	310.412	308.621	298	13.6
13.3[mm].1[mm]	314.936	313.471	311.666	314.936	313.468	311.709	308.587	298	7.56
39.3[mm].1[mm]	312.186	310.765	309.094	312.186	310.763	309.109	309.02	298	17.1
26.3[mm].0.5[mm]	313.821	312.406	310.275	313.821	312.405	310.306	308.749	298	13.557
26.3[mm].2[mm]	313.03	311.973	310.382	313.03	311.973	310.405	308.79	298	14.686

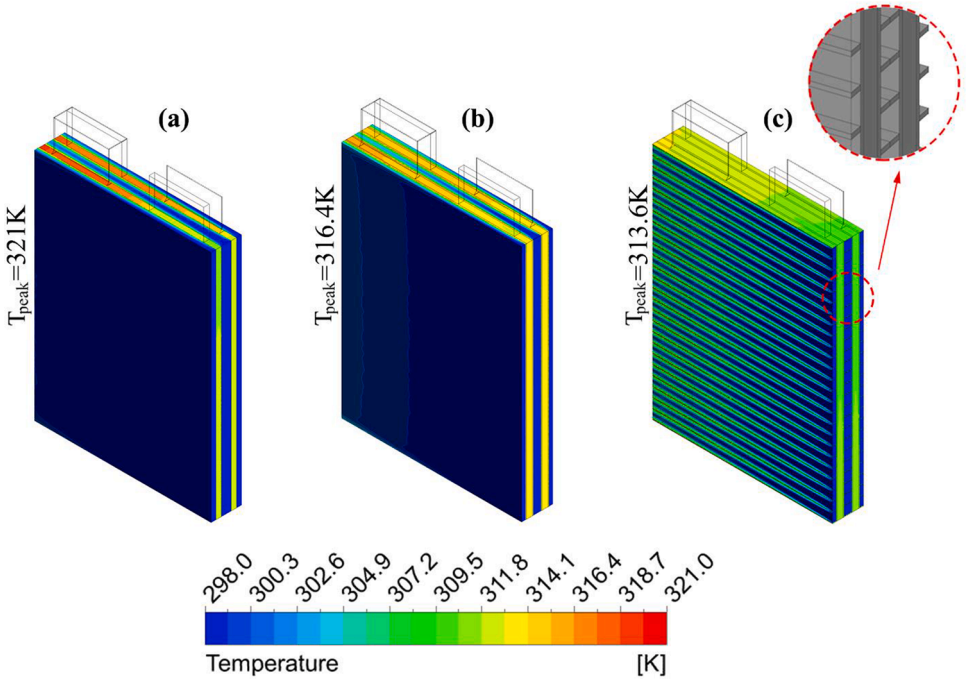

Fig. 6. Temperature distributions of battery cells at 10C discharge rate for (a) no fin structure, (b) structure of aluminum plate and (c) optimum fin structure case (26 fins with length of 3 mm and thickness of 1 mm).

on the cells become uniform as fins increases the heat transfer rate from the surface to the air as well as enabling lateral heat transfer to eliminate hot spots occurring on the battery surfaces.

3.1. Concept validation experiment

To prove the accuracy of numerical studies and validate developed manifold design, an experiment with the same design concept was established, as shown in Fig. 8(a). In the experimental setup, a battery pack of 25.2 V and 7.5 Ah was designed by using 7.5 Ah Kokam pouch cells connected as series and controlled by a battery management system. The battery pack was discharged at 300 K ambient temperature under 2 C-rate (15A) by BK Precision 8614 programmable electronic load. The temperatures were measured by K-type thermocouples and recorded by HIOKI-LR8431-20 datalogger. The thermocouples were placed on centre of each cell, in inlet and outlet regions of the manifold, and also in ambient. Bi-sonic 120 × 120 mm tube-axial fan was integrated with honeycombs to provide cooling air with the measured air velocity of 2.5m/s. The same conditions provided in the experimental setup were also simulated numerically. In the numerical study, the same methodology was applied as the previous numerical studies mentioned in this paper.

As can be seen in Fig. 8(b), experimental and numerical results are in good agreement with each other during operation. In experimental study, the maximum battery temperature and temperature difference between the cells are measured as 305.4 K and 1 K, respectively. This result alone shows that the elevated battery positioning concept can provide uniform flow distribution between the cells and yields uniform temperature distribution in the pack. In addition, comparison of experimental and numerical results show that the deviation of maximum battery temperature is around 1.5 K (Fig. 8(b),(c)) which heavily occurs near the end of discharge process. Overall, experiments show that the elevated battery positioning concept yield temperature uniformity in the pack and numerical procedure of the paper is valid and applicable.

4. Conclusion

In this study, the compact manifold design which was developed in our previous study as specified for the lithium-ion battery pack (15S1P) was investigated numerically at various inlet velocities, inlet temperatures and C-rates. The maximum battery temperatures exceed the desired temperature range without forced convection and/or elevated battery positioning in the manifold for fast and ultra-fast C-rate values. The maximum temperature increases remarkably around the positive tab of the cell during discharge. In addition, the maximum temperature difference between the batteries in the pack increases up to 14 K without forced convection. Accordingly, it is proved that the active cooling in battery packs is a requirement. Three-dimensional simulations show that the variation on the inlet velocity does not greatly affect the flow rate distribution among the channels in the developed manifold design. The average flow rate deviations from the average flow rates in each case are less than 2%. Except the last two channels, the average flow rate deviation from the average flow rate is 1.3% for the worst case. In addition, the developed manifold design provides significant cooling as C-rate increases to the ultra-fast order. However, the maximum battery temperature cannot be kept between the allowed operational temperature range at 10C discharge rate. Integration of fins between the battery cells enhances heat transfer from the cells to the air by increasing the heat transfer surface area. Even though fins increase the resistance to the flow of air, the interface of battery surfaces and fins enhances temperature distribution uniformity because fins enable lateral conduction to eliminate hot spots. An experimental study was conducted to prove the validity of both numerical procedure and elevated battery positioning concept to achieve uniform temperature distribution.

The results show that air cooling can be an effective thermal management system if elevated battery positioning concept is used. The results also show that fins would be required if the C-rate exceeds a limit value, more than 6C. If the maximum C-rate is less than 3 then no fin and no additional plates on the battery surfaces would be required to keep battery cells in the desired temperature range. These highlight that elevated battery positioning is essential for achieving uniform temperature distribution and increase in volumetric heat generation which

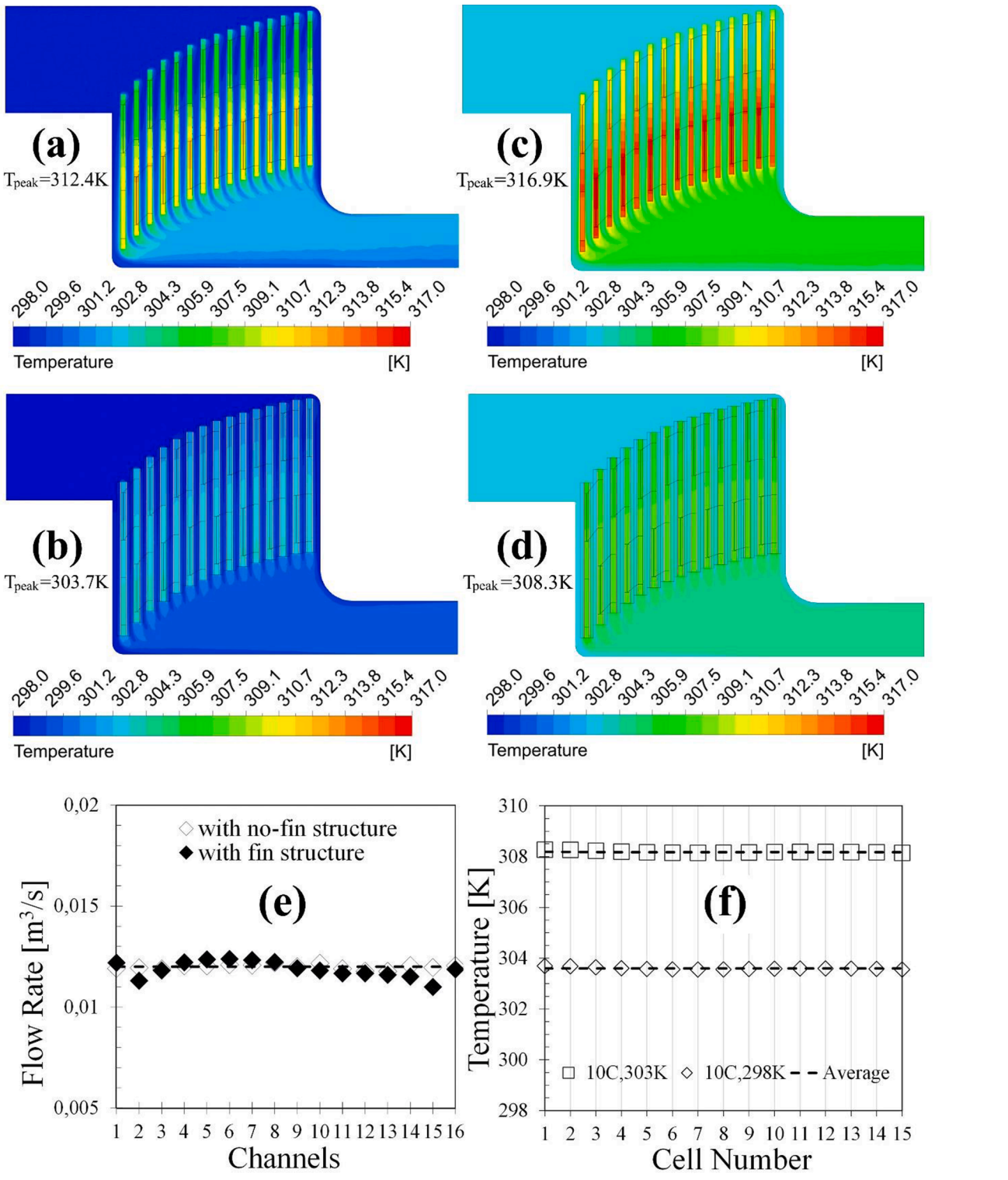

Fig. 7. Temperature distribution in battery pack at 10C discharge rate with inlet conditions of 298 K, 10 m/s for (a) no-fin case and (b) fin length of 3 mm case, and with inlet conditions of 303 K, 10 m/s for (c) no-fin case and (d) fin length of 3 mm case. (e) flow rate variations in channels and (f) maximum battery temperatures in the pack with fin structure at 10C for 10 m/s inlet velocity.

occurs at relatively high C-rates would require addition of fins and plates to keep the maximum temperature less than the desired temperature limit. Overall, this paper documents that the developed manifold design satisfies the requirements of advanced electric vehicle battery packs to prolong the battery lifetime as well as eliminating any risks related with failure such as thermal runaway.

CRediT authorship contribution statement

Sinan Gocmen: Conceptualization, Methodology, Validation, Formal analysis, Visualization, Writing – original draft. **Erdal Cetkin:** Supervision, Conceptualization, Methodology, Writing – review & editing.

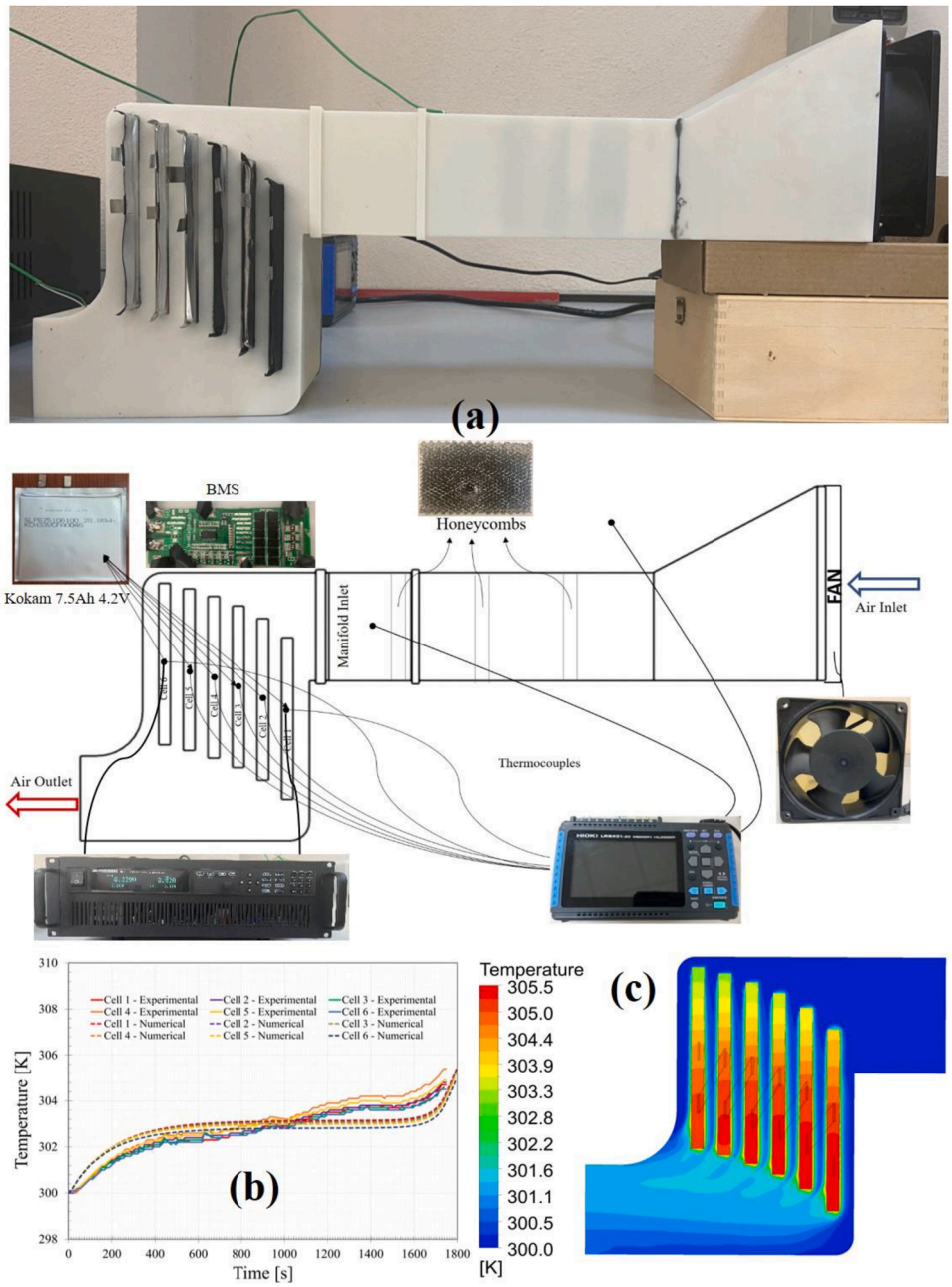

Fig. 8. (a) Picture and schematic of experimental setup, (b) Comparison of experimental and numerical temperature data, (c) temperature distribution of numerical study

Declaration of Competing Interest

None.

Acknowledgement

This research was funded by the Scientific and Technological Research Council of Turkey (TUBITAK) under grant number 218M498.

References

[1] B. Diouf, R. Pode, Potential of lithium-ion batteries in renewable energy, Renew. Energy (2015), https://doi.org/10.1016/j.renene.2014.11.058.
[2] B. Dunn, H. Kamath, J.M. Tarascon, Electrical energy storage for the grid: a battery of choices, Science (2011), https://doi.org/10.1126/science.1212741.
[3] J. Jaguemont, L. Boulon, Y. Dubé, A comprehensive review of lithium-ion batteries used in hybrid and electric vehicles at cold temperatures, Appl. Energy (2016), https://doi.org/10.1016/j.apenergy.2015.11.034.
[4] L. Ji, Z. Lin, M. Alcoutlabi, X. Zhang, Recent developments in nanostructured anode materials for rechargeable lithium-ion batteries, Energy Environ. Sci. (2011), https://doi.org/10.1039/c0ee00699h.
[5] Y. Ji, Y. Zhang, C.Y. Wang, Li-ion cell operation at low temperatures, J. Electrochem. Soc. 160 (4) (2013) A636–A649, https://doi.org/10.1149/2.047304jes.
[6] X. Liu, Z. Chen, C. Zhang, J. Wu, A novel temperature-compensated model for power Li-ion batteries with dual-particle-filter state of charge estimation, Appl. Energy (2014), https://doi.org/10.1016/j.apenergy.2014.02.072.
[7] Y.F. Wang, J.T. Wu, Performance improvement of thermal management system of lithium-ion battery module on purely electric AUVs, Appl. Therm. Eng. 146 (Jan. 2019) 74–84, https://doi.org/10.1016/j.applthermaleng.2018.09.108.
[8] T.F. Fuller, J.N. Harb, Electrochemical engineering /Thomas F. Fuller, 1, Georgia Institute of Technology, US, 2018. John N. Harb, (Brigham Young University, US).
[9] G. Piłatowicz, A. Marongiu, J. Drillkens, P. Sinhuber, D.U. Sauer, A critical overview of definitions and determination techniques of the internal resistance using lithium-ion, lead-acid, nickel metal-hydride batteries and electrochemical

double-layer capacitors as examples, J. Power Sources 296 (2015) 365–376, https://doi.org/10.1016/j.jpowsour.2015.07.073.
[10] D. Linden, T.B. Reddy, Handbook of batteries, 33, Mcgraw-Hill, 1995.
[11] H. Feng, D. Song, A health indicator extraction based on surface temperature for lithium-ion batteries remaining useful life prediction, J. Energy Storage 34 (2021), 102118, https://doi.org/10.1016/j.est.2020.102118.
[12] Q. Wang, B. Jiang, B. Li, Y. Yan, A critical review of thermal management models and solutions of lithium-ion batteries for the development of pure electric vehicles, Renew. Sustain. Energy Rev. (2016), https://doi.org/10.1016/j.rser.2016.05.033.
[13] B. Scrosati, J. Garche, Lithium batteries: Status, prospects and future, J. Power Sources (2010), https://doi.org/10.1016/j.jpowsour.2009.11.048.
[14] Z. Rao, S. Wang, A review of power battery thermal energy management, Renew. Sustain. Energy Rev. (2011), https://doi.org/10.1016/j.rser.2011.07.096.
[15] P.G. Balakrishnan, R. Ramesh, T.P. Kumar, Safety mechanisms in lithium-ion batteries, J. Power Sources (2006), https://doi.org/10.1016/j.jpowsour.2005.12.002.
[16] X. Feng, M. Ouyang, X. Liu, L. Lu, Y. Xia, X. He, Thermal runaway mechanism of lithium ion battery for electric vehicles: a review, Energy Storage Mater. (2018), https://doi.org/10.1016/j.ensm.2017.05.013.
[17] Federal Aviation Authority, "Events with smoke, fire, extreme heat or explosion involving lithium batteries. [Online]. Available: https://www.faa.gov/hazmat/resources/lithium_batteries/media/Battery_incident_chart.pdf, 2021 (accessed 3 November 2021).
[18] M. Doyle, Modeling of galvanostatic charge and discharge of the lithium/polymer/insertion cell, J. Electrochem. Soc. (1993), https://doi.org/10.1149/1.2221597.
[19] Y. Chen, Heat transfer phenomena in lithium/polymer-electrolyte batteries for electric vehicle application, J. Electrochem. Soc. (1993), https://doi.org/10.1149/1.2220724.
[20] Y. Chen, Thermal analysis of lithium-ion batteries, J. Electrochem. Soc. (1996), https://doi.org/10.1149/1.1837095.
[21] Y. Chen, Three-dimensional thermal modeling of lithium-polymer batteries under galvanostatic discharge and dynamic power profile, J. Electrochem. Soc. (1994), https://doi.org/10.1149/1.2059263.
[22] V. Srinivasan, C.Y. Wang, Analysis of Electrochemical and Thermal Behavior of Li-Ion Cells, J. Electrochem. Soc. (2003), https://doi.org/10.1149/1.1526512.
[23] K.H. Kwon, C.B. Shin, T.H. Kang, C.S. Kim, A two-dimensional modeling of a lithium-polymer battery, J. Power Sources (2006), https://doi.org/10.1016/j.jpowsour.2006.03.012.
[24] U. Seong Kim, J. Yi, C.B. Shin, T. Han, S. Park, Modeling the dependence of the discharge behavior of a lithium-ion battery on the environmental temperature, J. Electrochem. Soc. (2011), https://doi.org/10.1149/1.3565179.
[25] T.M. Bandhauer, S. Garimella, T.F. Fuller, A critical review of thermal issues in lithium-ion batteries, J. Electrochem. Soc. (2011), https://doi.org/10.1149/1.3515880.
[26] A. Celik, H. Coban, S. Göcmen, M.A. Ezan, A. Gören, A. Erek, Passive thermal management of the lithium-ion battery unit for a solar racing car, Int. J. Energy Res. 43 (8) (2019), https://doi.org/10.1002/er.4521.
[27] R. Kizilel, A. Lateef, R. Sabbah, M.M. Farid, J.R. Selman, S. Al-Hallaj, Passive control of temperature excursion and uniformity in high-energy Li-ion battery packs at high current and ambient temperature, J. Power Sources (2008), https://doi.org/10.1016/j.jpowsour.2008.04.050.
[28] N. Javani, I. Dincer, G.F. Naterer, B.S. Yilbas, Heat transfer and thermal management with PCMs in a Li-ion battery cell for electric vehicles, Int. J. Heat Mass Transf. (2014), https://doi.org/10.1016/j.ijheatmasstransfer.2013.12.076.
[29] Z. Rao, Z. Qian, Y. Kuang, Y. Li, Thermal performance of liquid cooling based thermal management system for cylindrical lithium-ion battery module with variable contact surface, Appl. Therm. Eng. (2017), https://doi.org/10.1016/j.applthermaleng.2017.06.059.
[30] L.H. Saw, Y. Ye, A.A.O. Tay, W.T. Chong, S.H. Kuan, M.C. Yew, Computational fluid dynamic and thermal analysis of Lithium-ion battery pack with air cooling, Appl. Energy (2016), https://doi.org/10.1016/j.apenergy.2016.05.122.
[31] H. Park, A design of air flow configuration for cooling lithium ion battery in hybrid electric vehicles, J. Power Sources (2013), https://doi.org/10.1016/j.jpowsour.2013.03.102.
[32] X.M. Xu, R. He, Research on the heat dissipation performance of battery pack based on forced air cooling, J. Power Sources (2013), https://doi.org/10.1016/j.jpowsour.2013.03.004.
[33] Y. Liu, J. Zhang, Design a J-type air-based battery thermal management system through surrogate-based optimization, Appl. Energy 252 (Oct. 2019), 113426, https://doi.org/10.1016/j.apenergy.2019.113426.
[34] H. Sun, R. Dixon, Development of cooling strategy for an air cooled lithium-ion battery pack, J. Power Sources (2014), https://doi.org/10.1016/j.jpowsour.2014.08.107.
[35] E. Cetkin, Constructal microdevice manifold design with uniform flow rate distribution by consideration of the tree-branching rule of leonardo da vinci and hess-murray rule, J. Heat Transf. (2017), https://doi.org/10.1115/1.4036089.
[36] J. Zhang, H. Kang, K. Wu, J. Li, Y. Wang, The impact of enclosure and boundary conditions with a wedge-shaped path and air cooling for battery thermal management in electric vehicles, Int. J. Energy Res. 42 (13) (2018) 4054–4069, https://doi.org/10.1002/er.4122.
[37] T. Wang, K.J. Tseng, J. Zhao, Z. Wei, Thermal investigation of lithium-ion battery module with different cell arrangement structures and forced air-cooling strategies, Appl. Energy (2014), https://doi.org/10.1016/j.apenergy.2014.08.013.
[38] K. Chen, S. Wang, M. Song, L. Chen, Structure optimization of parallel air-cooled battery thermal management system, Int. J. Heat Mass Transf. (2017), https://doi.org/10.1016/j.ijheatmasstransfer.2017.04.026.
[39] J. Zhang, X. Wu, K. Chen, D. Zhou, M. Song, Experimental and numerical studies on an efficient transient heat transfer model for air-cooled battery thermal management systems, J. Power Sources 490 (2021), 229539, https://doi.org/10.1016/j.jpowsour.2021.229539.
[40] S. Pan, C. Ji, S. Wang, B. Wang, Study on the performance of parallel air-cooled structure and optimized design for lithium-ion battery module, Fire Technol. 56 (6) (2020) 2623–2647, https://doi.org/10.1007/s10694-020-01020-x.
[41] S. Maharudrayya, S. Jayanti, A.P. Deshpande, Flow distribution and pressure drop in parallel-channel configurations of planar fuel cells, J. Power Sources (2005), https://doi.org/10.1016/j.jpowsour.2004.12.018.
[42] C. Li, Y. Li, L. Gao, A. Garg, W. Li, Surrogate model-based heat dissipation optimization of air-cooling battery packs involving herringbone fins, Int. J. Energy Res. 45 (6) (2021) 8508–8523, https://doi.org/10.1002/er.6387.
[43] S. Gocmen, S. Gungor, E. Cetkin, Thermal management of electric vehicle battery cells with homogeneous coolant and temperature distribution, J. Appl. Phys. 127 (23) (2020), 234902, https://doi.org/10.1063/5.0004453.
[44] Ansys® Fluent, Release 2021R1, Help System, ANSYS Fluent Theory Guide, ANSYS, Inc.
[45] H. Gu, Mathematical analysis of a Zn/NiOOH cell, J. Electrochem. Soc. (1983), https://doi.org/10.1149/1.2120009.
[46] L. Yiwei, Q. Yuping, Z. Zezhi, Z. Yangjun, Simulation and analysis of operating characteristics of power battery for flying car utilization, eTransportation 8 (2021) 100111, https://doi.org/10.1016/j.etran.2021.100111.
[47] D. Ti, P. Peng, J. Fangming, Numerical modeling and analysis of the thermal behavior of NCM lithium-ion batteries subjected to very high C-rate discharge/charge operations, Int. J. Heat and Mass Transfer 117 (2018) 261–272, https://doi.org/10.1016/j.ijheatmasstransfer.2017.10.024.
[48] B. Hamidreza, K. Danial, B. Mohammadreza, J. Joris, G. Morteza, B. Masud, B. Maitane, M. Joeri Van, Thermal management analysis using heat pipe in the high current discharging of lithium-ion battery in electric vehicles, J. Energy Storage 32 (2020) 101893, https://doi.org/10.1016/j.est.2020.101893.
[49] B. Hamidreza, K. Danial, J. Joris, H.G. Foad, K. Theodoros, B. Maitane, M. Joeri Van, Novel thermal management methods to improve the performance of the Li-ion batteries in high discharge current applications, Energy 224 (2021) 120165, https://doi.org/10.1016/j.energy.2021.120165.